Emergent Properties of Antiagglomerant Films Control Methane Transport: Implications for Hydrate Management

François Sicard[1],* Tai Bui[1], Deepak Monteiro[2], Qiang Lan[2], Mark Ceglio[2], Charlotte Burress[2], and Alberto Striolo[1]

[1] *Department of Chemical Engineering, University College London, WC1E 7JE, London, UK and*
[2] *Halliburton, Houston, Texas, USA*

The relation between collective properties and performance of antiagglomerants (AAs) used in hydrate management is handled using molecular dynamics simulations and enhanced sampling techniques. A thin film of AAs adsorbed at the interface between one flat sII methane hydrate substrate and a fluid hydrocarbon mixture containing methane and n-dodecane is studied. The AA considered is a surface-active compound with a complex hydrophilic head that contains both amide and tertiary ammonium cation groups and hydrophobic tails. At sufficiently high AA density, the interplay between the surfactant layer and the liquid hydrocarbon excludes methane from the interfacial region. In this scenario, we combine metadynamics and umbrella sampling frameworks to study accurately the free-energy landscape and the equilibrium rates associated with the transport of one methane molecule across the AA film. We observe that local configurational changes of the liquid hydrocarbon packed within the AA film are associated with high free-energy barriers for methane transport. The time scales estimated for the transport of methane across the AA film can be, in some cases, comparable to those reported in the literature for the growth of the hydrates, suggesting that one possible mechanism by which AAs delay the formation of hydrate plugs could be providing a barrier to methane transport. Considering the interplay between structural design and collective properties of AAs might be of relevance to improve their performance in flow assurance.

Keywords: antiagglomerant, gas hydrate management, flow assurance, numerical simulations, metadynamics, free-energy landscape, transition rates

INTRODUCTION

Gas hydrates, also known as clathrate hydrates, are ice-like inclusion compounds consisting of polyhedral hydrogen-bonded water cages stabilized by guest gas molecules [1–3]. They are not chemical compounds because no strong chemical bonds exist between water and gas molecules [4, 5]. They are formed under high-pressure and low-temperature conditions such as those found in deep oceans and pipelines [6]. The gas molecules able to be trapped (enclathrated) into the water cages are usually small (< 10 Å): methane, ethane, propane, 1-butane, nitrogen, hydrogen, and carbon dioxide [7]. Clathrate hydrates are relevant in a variety of scientific and industrial contexts, including climate change modeling [8], carbon dioxide sequestration [9], hydrocarbon extraction [10], hydrogen and natural gas storage [10–12], separation and refrigeration technologies [13], marine biology [14], and planetary surface chemistry [15]. Of particular interest are the hydrocarbon hydrates that can form blockages in oil and gas pipelines [3, 16]. This phenomenon severely affects the safety of pipeline flow assurance [16].

Three major stages are associated with hydrate plug formation: nucleation [3, 17], growth [3, 18], and agglomeration [19, 20]. Numerous experimental investigations [3, 21–26], modeling, and simulations [27–31] have contributed to the current understanding of such stages. As offshore drilling activities have moved towards geological sites of deeper waters and colder tempera-

tures [32], the community is facing ever-more severe technical challenges. To manage hydrates in pipelines, hydrate inhibitors are used. They are differentiated depending on their mode of action: thermodynamic hydrate inhibitors (TIs) [10], such as methanol and monoethylene glycol, shift the stability conditions of hydrates to lower temperatures and higher pressures, but require large amounts (10 to 50 wt%) to be effective. Low dosage hydrate inhibitors (LDHIs) [2] instead are effective at concentrations as low as 1 wt% of water. LDHIs were introduced in the mid-1980s and early 1990s [33]. Unlike TIs, LDHIs do not influence the thermodynamics of hydrates formation but affect its kinetics [2]. Kinetic hydrate inhibitors (KHIs) and anti-agglomerants (AAs) are the two main LDHIs classes [34]. Most KHIs are polymeric compounds containing amide groups, such as poly(N-vinylpyrrolidone), polyvinyl-caprolactam, and polydiethylacrylamide [2, 35]. They are believed to delay hydrate nucleation and/or growth. AAs, mostly surface-active surfactants, are usually amphiphilic chemicals with complex hydrophobic tails and hydrophilic headgroups [36]. They allow the hydrate particles to form but keep them dispersed, yielding transportable slurries [2, 16, 37]. When AAs adsorb at the oil-hydrate interface, the hydrophobic tails preferably point toward the hydrocarbon phase, possibly inducing an effective repulsion when two hydrates approach each other [3, 38, 39]. When the AAs polar headgroups are adsorbed on the hydrate surface, they could interfere with the hydrate growth [37, 40]. Quaternary ammonium salts, first developed by Shell in the early 1990s, are the

most well-known AAs [41]. Promising performance of commercial additives and new AAs have been reported by several research groups [37, 42–46]. Most AAs are only effective at low water content (e.g., less than 30%), but some can be effective at high water content (up to 80%), such as those reported by Gao [47]. While the use of AAs is increasing in subsea projects across the industry [48], their mechanisms of action remain poorly understood. Such understanding is necessary to improve their cost effectiveness and expand the range of conditions over which their use is safe and convenient.

Because classical molecular dynamics (MD) simulations can follow the trajectories of individual molecules, MD has been the preferred technique to investigate the formation of hydrates with and without the presence of KHIs [4, 5, 36, 39, 49–51]. Recent numerical studies have concentrated on the relation between structure and performance of model AAs, with the emergent molecular-level characterization of the surface adsorption mechanisms of surfactants to hydrates considered as a signature of *microscopic* performance [52, 53]. The coalescence mechanisms of gas hydrate crystals and water droplet have also been studied [39]. Recently, Bui et al. [36] related the *macroscopic* performance of a class of AAs in flow-assurance applications to the molecular-level properties of the surfactant interfacial film. Those simulations, compared to experiments, suggested that effective AAs could provide energy barriers in methane transport.

In the present work, the authors quantify such energy barriers as experienced by one methane molecule diffusing from the hydrocarbon phase to the growing hydrate. Building on the work of Bui et al. [36], we consider the AA that is most effective at excluding methane from the film of AAs formed at the water-hydrocarbon interface. This AA was determined to have good performance in laboratory tests designed to screen AAs for flow assurance applications. The metadynamics [54] (metaD) and umbrella sampling [55] (US) frameworks are combined to study accurately the free-energy (FE) landscape and the equilibrium rates associated with the transport mechanisms of one *free* methane molecule across a densely packed interfacial layer. At sufficiently high AA density, we show that the FE barrier is caused by local configurational changes of the liquid hydrocarbon molecules packed within the AA film.

METHODS

Unbiased MD simulations

MD simulations were performed with the GROMACS software package, version 5.1.1 [56] using the TIP4P/Ice water model [57]. Biased simulations were performed using version 2.3 of the plugin for FE calculation, PLUMED [58]. The TIP4P/Ice model has been successfully implemented to study hydrate nucleation and growth [4, 59] and to investigate the performance of potential hydrate inhibitors [60]. This model yields an equilibrium temperature for the formation of gas hydrates at high pressure close to experimental values [61]. Methane and n-dodecane were represented within the united-atom version of the TraPPE-UA force field [62]. AAs were modeled using the general Amber force field (GAFF) [63], which is often implemented for modeling organic and pharmaceutical molecules containing H, C, N, O, S, P, and halogens. Atomic charges were calculated with the AM1-BCC method employed in Antechamber from the Amber 14 suite [64]. The chloride counterions (Cl^-) were modeled as charged Lennard-Jones (LJ) spheres with the potential parameters taken from Dang [65], without polarizability. The sII hydrates were considered to be the solid substrate, and they were not allowed to vibrate in this work. AAs, chloride counterions, n-dodecane, and methane composed the liquid phase. Dispersive and electrostatic interactions were modeled by the $12-6$ LJ and Coulombic potentials, respectively. The Lorentz-Berthelot mixing rules [66, 67] were applied to determine the LJ parameters for unlike interactions from the parameters of the pure components. The distance cutoff for all non-bonded interactions was set to 1.4 nm. Long-range corrections to the electrostatic interactions were described using the particle mesh Ewald (PME) method [68–70] with a Fourier grid spacing of 0.12 nm, a tolerance of 10^{-5}, and fourth-order interpolation. Periodic boundary conditions were applied in three dimensions for all simulations.

To construct the initial configurations, we followed the procedure described by Bui et al. [36]. The unit cell of sII methane hydrates was adapted from the study of Takeuchi et al. [71]. The sII methane hydrate unit cell was replicated three times in the X and Y directions (5.193 nm) and two times in the Z direction (3.462 nm). It was then flanked by a thin liquid water film of approximately 0.5 nm on both sides along the Z direction. The desired number of AA molecules was arranged near both sides of the hydrate substrate. The chloride counterions (Cl^-) were placed next to the AA headgroups. The n-dodecane and methane molecules were placed within the remainder of the simulation box. The time step used in all the simulations was 0.001 ps, and the list of neighbors was updated every 0.01 ps with the *grid* method and a cutoff radius of 1.4 nm.

The energy of the model was first optimized with the "steepest descent minimization" algorithm to remove high-energy configurations. Subsequently, to minimize the possibility that the initial configuration biased the simulation results, an NVT temperature-annealing procedure, as implemented in GROMACS [56], was con-

ducted. The algorithm linearly decreased the system temperature from 1000 K to 277 K in 500 ps. In these simulations, the hydrate substrate and chloride ions were kept frozen. To relax the structure of n-dodecane and AAs, a NVT simulation was conducted at 277 K for 2 ns using the Berendsen thermostat [72], with the sII hydrate structure kept frozen. The equilibration phase was then conducted within the isobaric-isothermal (NPT) ensemble under thermodynamic conditions favorable for hydrate formation ($T = 277$ K and $P = 20$ MPa) to equilibrate the density. During the NPT simulation, all molecules in the system were allowed to move, including water and methane molecules in the hydrate substrate. The pressure coupling was applied only along the Z direction of the simulation box, which allowed the X and Y dimensions to be maintained constant. Temperature and pressure were maintained at 277 K and 20 MPa, respectively using the Berendsen thermostat and barostat [72] for 5 ns. This is considered the most efficient algorithm to scale simulation boxes at the beginning of a simulation [73]. We then switched to the Nose-Hoover thermostat [74] and the Parrinello-Rahman barostat [75] for 100 ns, which are considered more thermodynamically consistent algorithms [73]. This numerical protocol allowed the AAs to assemble and orient to form the ordered layer described in the work of Bui et al. [36]. The system was then equilibrated for 3 ns in NVT conditions coupling with the *v-rescale* thermostat [76] ($T = 277$ K, $\tau_T = 0.1$ ps). To define the position of the *free* methane molecule in the simulation box with respect to the sII hydrate structure, the simulation was continued in NVT conditions holding in place the methane molecule enclathrated into the water cages defining the sII hydrate structure, as implemented with the *freeze group* procedure in GROMACS [56].

Biased MD simulations

The phenomenon of interest (*i.e.* the transport of methane across the interfacial layer) occurs on time scales that are orders of magnitude longer than the accessible time that can be currently simulated with classical MD simulations. A variety of methods, referred to as *enhanced sampling techniques* [77–81], can be implemented to overcome this limitation. These methods accelerate rare events and are based on constrained MD. MetaD [54, 82–84] and US [55, 85] belong to this class of methods: they enhance the sampling of the conformational space of a system along a few selected degrees of freedom, named reaction coordinates or collective variables (CVs), and reconstruct the probability distribution as a function of these CVs. These techniques are proven powerful tools to study biological [86–89] and chemical systems [90–92]. However, despite these successes, care should be taken to properly choose and implement the reaction coordinates [82–84].

We first ran a well-tempered metaD (WT-metaD) simulation [93, 94] using the three Cartesian coordinates (X, Y and Z) of the *free* methane molecule as CVs. WT-metaD is a method based on a biasing of the potential surface. The biasing potential is dynamically placed on top of the underlying potential energy landscape to discourage the system from visiting the same points in the configurational space. The WT-metaD time-dependent bias, $V_{\text{bias}}(s,t)$ can have any form, but a Gaussian potential is usually implemented [82]:

$$V_{\text{bias}}(s,t) = \omega \sum_{t'<t} \exp\left[- \frac{(s(t) - s(t'))^2}{2\sigma^2} \right]. \quad (1)$$

In Eq. 1, ω is the height of the biasing potential, σ is the width, t is the time, and s is the collective variable. Following the algorithm introduced by Barducci et al. [93], a Gaussian-shaped potential is deposited every $\tau_G = 2$ ps, with height $\omega = \omega_0 e^{-V(s,t)/(f-1)T}$, where $\omega_0 = 5$ kJ/mol is the initial height, T is the temperature of the simulation, and $f \equiv (T + \Delta T)/T = 25$ is the bias factor with ΔT a parameter with the dimension of a temperature.

In our implementation, the resolution of the recovered FE surface is determined by the width of the Gaussian $\sigma = 0.25$ nm along the X, Y and Z directions. This step was motivated by the inherent competition between different pathways that can lead to methane transport through the AA layer, with each path characterized by different FE barriers. WT-metaD simulations were run restraining the position of the AA layer while allowing the hydrocarbon molecules, both trapped at the interface and present in the bulk phase, to move freely. This was necessary to minimize *local* hysteresis effects that would occur in the *global* convergence of the WT-metaD resulting from the flexibility of the AA layer in defining the Cartesian position of the *free* methane molecule with respect to the AA film.

Once the possible pathways across the AA film were identified, the potential of mean force (PMF) along them was rigorously calculated using US. This combined metaD/US approach, originally proposed by Zhang and Voth [95] in the biophysical context, provides a powerful means to calculate a physically meaningful PMF where the convergence problem, sometimes associated with metaD, is avoided. The approach also avoids the discontinuity problem, often associated with US calculations that assume a straight-line reaction coordinate, yielding a physically accurate PMF [95]. It is worth noting that in the combined metaD/US approach, the final PMF is not sensitive to the choice of the WT-metaD parameters, as long as they are in reasonable range because the PMF is not directly calculated from metaD [95]. In the WT-metaD simulations, soft walls were added on both side of the interfacial layer to limit sampling inside the

AA film.

Once representative pathways were identified, we calculated the associated PMF using US, with the $Z-$ Cartesian coordinate along the preliminary pathways as collective variable. The system was free in the $X - Y$ plane. To design the US windows, it is common practice to implement one of two approaches: 1) the system is dragged using the steered dynamics [85] or 2) the initial structures are prepared by changing the position of the CV directly followed by energy minimization [96]. As discussed by Nishizawa [96], it is possible, with these protocols, to drive the system into configurations with no reverse transition (*i.e.*, breaking the ergodicity of the system). This can be particularly true with fluid/soft systems, where covalent bonds are not present. This shortcoming can be associated to *artifactual* kinetic barriers between consecutive states that slow sampling of configurations during US. These effects could render the free-energy profile (FEP) analysis inappropriate and/or unfeasible using a reasonable amount of computation. To avoid these shortcomings, we used the adiabatic biased molecular dynamics (ABMD) framework, which is based on the local fluctuations of the system [97–100] .

Furthermore, one must avoid inefficient sampling in the CV orthogonal degrees of freedom (either $X-$ or $Y-$ direction), despite ensuring good overlap in the $Z-$ direction. As others indicated [95, 101, 102], this numerical issue could cause a discontinuity in configurational space that would introduce PMF errors. To ensure the results are reliable, we controlled the efficiency of the sampling along the CV orthogonal degrees of freedom with the implementation of the *flat-bottomed* potential [95, 101, 102]

$$V_{fb}(q) = \frac{1}{2} k_{fb} \Theta \big[\rho(q) - R_{fb} \big] \big(\rho(q) - R_{fb} \big)^2, \quad (2)$$

where q denotes the $X-$ or $Y-$ direction, $\rho(q)$ the distance from the path along which the US windows are distributed, k_{fb} the harmonic force constant, $\Theta(q) \equiv 1 - \Pi(q)$ with $\Pi(q)$ the rectangular function, and R_{fb} the confinement radius. No constraint was added in the $X - Y$ plane in the present PMF calculations using the Z-coordinate as CV, unless the methane molecule is close to the bulk solvent or the hydrate. Therefore, as $V_{fb}(q)$ is *flat-bottomed*, it has no effect when the methane molecule travels through the interfacial layer. This bias only affects the overall offset of the reconstructed FEP in the layer and not its shape [102].

Upon completion of the US simulations, FEPs were calculated from the final 4 ns of simulation time using the weighted histogram analysis method (WHAM) [103]. Statistical error analysis was conducted using the integrated Monte Carlo bootstrapping framework [104], implemented in WHAM [103], as discussed in the Supporting Information (SI).
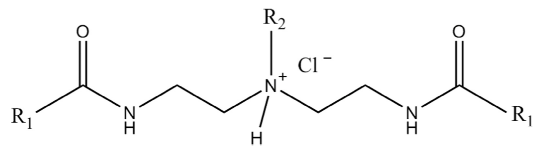

FIG. 1. Molecular structure of the AA with two long tails R_1 (*n*-dodecyl) and one short tail R_2 (*n*-butyl).

To estimate the rate of the methane transport across the interfacial layer, we extended the *standard* scope of WT-metaD considering the recent method or Parrinello, Salvalaglio and Tiwary [105, 106]. This technique has been applied to study transition rates in biological and chemical systems [89, 107–112]. We denote by τ the *physical* mean transition time for the methane to pass over the energy barrier and by τ_M the mean transition time obtained from the WT-metaD run. The latter is linked to the *physical* mean transition time, τ, by means of the acceleration factor,

$$\alpha(t) = \tau/\tau_M = \langle e^{\beta V_{\mathrm{bias}}(s,t)} \rangle_M , \quad (3)$$

where the angular brakets denote an average over a WT-metaD run confined to a metastable basin, and $V_{\mathrm{bias}}(s,t)$ is the WT-metaD time-dependent bias defined in Eq. 1. To avoid depositing bias in the transition state region, we increase the time lag between two successive Gaussian depositions in the WT-metaD framework, $\tau_G = 400$ ps [105, 106]. We confirmed that the statistics of transition times follows a Poisson distribution, performing a two-sample Kolmogorov-Smirnov (KS) test. The compliance to the KS test allowed us to asses the reliability of the CV considered to distinguish between the different metastable states within the US framework [105, 106] and to reconstruct accurately the PMFs.

RESULTS AND DISCUSSION

Interfacial structure

The molecular structure of the AA considered in this study is shown in Fig. 1, with R_1 and R_2 groups representing long and short tails in one AA, respectively. The AA molecule headgroup includes both amide and tertiary ammonium cation groups. Following the notation of Bui et al. [36], the AA are denoted as $S_X L_Y$, where $X = 4$ (*n*-butyl) and $Y = 12$ (*n*-dodecyl) indicate the number of carbon atoms in the short (S) and long (L) tail, respectively. The long AA tails become ordered, almost perpendicular to the hydrate surface, when the surface coverage increases, as previously reported by Bui et al. [36]. We consider a surface density ≈ 0.67 molecule/nm^2, sufficiently high to yield a dense ordered film at the hydrate-hydrocarbon interface and sufficiently

low to allow interface regions with both low and high AA density. To define *unambiguously* the spatial organization of the AA layer, the position of the central Nitrogen atom on each surfactant in Fig. 2 was fixed using a restraint potential, as implemented in GROMACS [56]. This additional numerical constraint does not impact the analysis of the transport properties of the *free* methane molecule through the AA layer as the AAs remain adsorbed at the hydrate-hydrocarbon interface within the timeframe of our MD simulations. The initial configuration used in the simulations is shown in Fig. 2.

To characterize the thermodynamic and dynamical properties of the AA film adsorbed at the interface between the flat sII methane hydrate and the hydrocarbon fluid, one must consider the non-isotropic distribution of the surfactant film at the interface. This spatial distribution depends on the AA concentration [36] and yields different pathways available to the passage of the *free* methane molecule. We quantified the *efficiency* of the AA layer in limiting the transport of the methane molecule with the identification of the *minimal* FE pathway. This analysis allowed for study of the transport mechanisms at play when one *free* methane molecule travels through the interface.

Identification of representative pathways

To identify representative pathways available to the methane molecule to cross the AA film, we ran WT-metaD simulations, as discussed previously. This approach was necessary to handle the non-isotropic distribution of the AAs within the interfacial layer. However, it did not prevent hysteresis effects caused by *local* reorganization of the liquid hydrocarbons within the AA layer. This hysteresis effect might occur when the bias potential becomes sufficiently high to expel hydrocarbon molecules from the interfacial layer. To prevent this possible shortcoming, one should consider an additional CV, accounting for the *local* behaviour of the liquid hydrocarbon molecules. This is well known, for instance, in biological docking studies [110, 113–115]. Computational limitations made it unfeasible to consider an additional CV in the present work.

Instead, we ran WT-metaD simulations to identify representative pathways. Figure 3 shows representative FEPs obtained within the WT-metaD framework, along with the respective snapshots to illustrate the different scenarios. The pathways identified occur in interfacial regions with different AA density. The *minimal* FEP corresponds to the diffusion of the methane through an interfacial region made up of a large cluster of hydrocarbons. These regions show a characteristic size $\approx 20\text{Å}$ in the simulations, which is comparable to the molecular dimension of the dodecane molecules (cf. Figure 3a).

When hydrocarbons are confined in these narrow regions, it is possible that the effective viscosity differs with respect to that in the bulk [116]. The *intermediate* FEP corresponds to the diffusion of the methane along the edge of a hydrocarbon cluster to the surrounding AA molecules. As shown in Figure 3b, the methane molecule travels through the interfacial layer and eventually interacts with the hydrophobic short tail of one AA, which can be parallel to the interfacial layer. This specific orientation enhances the interaction between the short tail and the methane molecule, stabilizing the system. This effect yields the *inversion* of the thermodynamic stability of the system with respect to the global ($Z/Z_{\text{box}} \approx 0.27$) and local ($Z/Z_{\text{box}} \approx 0.36$) minima observed along the *minimal* FEP. The *maximal* FEP corresponds to the diffusion of methane through a locally dense AA region, in which a few oil molecules are trapped within the AA layer (cf. Figure 3c). Possibly because the AA molecules are rigid in these simulations, the transport of methane across this region encounters a large FE barrier.

As discussed in the SI, the FEP obtained within the metadynamics framework shows the same qualitative behavior as the FEP obtained within the ABMD/US frame-
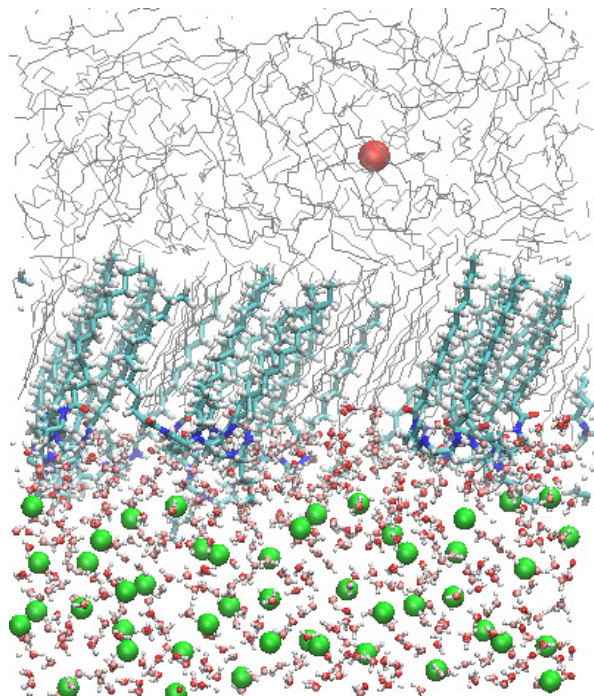

FIG. 2. Initial configuration obtained after equilibration for an AA surface density ≈ 0.67 molecule/nm^2. Green spheres represent methane molecules in the sII methane hydrate. Grey lines represent *n*-dodecane molecules, either in the bulk or trapped within the AA layer. The *free* methane molecule is shown as a red sphere. Yellow, red, blue, white, and cyan spheres represent chloride ions, oxygen, nitrogen, hydrogen, and carbon atoms in AA molecules, respectively. Only half of the simulation box is shown here for clarity.
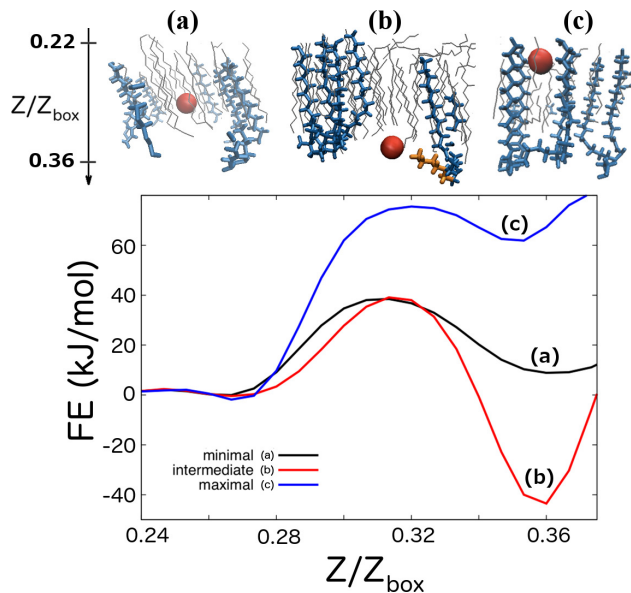
FIG. 3. Bottom: FEPs associated with three pathways obtained with the WT-metaD framework. Top: representative snapshots to illustrate the *minimal* (a), *intermediate* (b), and *maximal* (c) scenarios. Grey and blue lines represent *n*-dodecane and AA molecules, respectively. In the snapshots, the *free* methane molecule is shown as a red sphere. In (b), the AA short tail interacting with the methane molecule is colored orange. The *x*-axis corresponds to the *Z*-Cartesian coordinate of methane expressed in reduced units, Z/Z_{box}, with Z_{box} the size of the simulation box along the Z direction.

molecules induce the alignment and rigidity of the oil molecules within the interface, as shown in Figure 2 and reported by Bui et al. [36]. Freezing the AA molecules does not impact the location of global and local minima, $Z/Z_{box} = 0.27$ and $Z/Z_{box} = 0.36$, respectively, and the FE $\Delta F_0 \approx 8.5$ kJ/mol. This was expected as these quantities correspond to AA-free locations above and below the interfacial layer, which are not impacted by the AA freezing. However, freezing the AA molecules yields an increase of the FE barriers, $\Delta\Delta F \equiv \Delta F_c^{frozen} - \Delta F_c^{free} \approx 7.5$ kJ/mol at the transition, $Z/Z_{box} \approx 0.31$ (cf. Figure 4). This difference highlights the interplay between the rigidity of the AA layer and the *local pliability* of the oil molecules trapped within the interfacial layer.

Transport Mechanisms

Because the results obtained when the AA layer is flexible are more realistic, we further study the transport mechanism as observed within the US/ABMD framework. Figure 5 shows representative snapshots extracted from the FEP. The free methane molecule is initially in the bulk hydrocarbon phase, above the AA layer. When it comes closer to the interface, it is first trapped in a local FE minimum ($Z/Z_{box} \approx 0.27$). This minimum corresponds to a transition region between oil molecules isotropically oriented in the bulk and oil molecules parallel to the AA tails. The methane molecule then en-

work, with quantitative differences caused by numerical artifacts. The remainder of the paper discusses the analysis on the *minimal* FE pathway, which shows the lowest FE barriers for transport of methane from the hydrocarbon to the hydrate (capture) and from the hydrate to the hydrocarbon (escape). In the following detailed analysis, we implemented the US and ABMD frameworks, as described previously. The *minimal* FEP would provide the lowest boundary for time constants representative for methane transport across the AAs film.

Minimal free-energy pathway

Thermodynamic properties

Two different systems were compared: 1) the AA layer is kept frozen, as in the case of the preliminary WT-metaD simulation and 2) the AA layer is flexible, although the central nitrogen atom of each AA molecule remains frozen. The former approach allows us to define *unambiguously* the Cartesian position of the *free* methane molecule with respect to the AA layer. Figure 4 compares the FEP associated to the *minimal* FE path, as obtained in the two approaches. In both cases, the AA
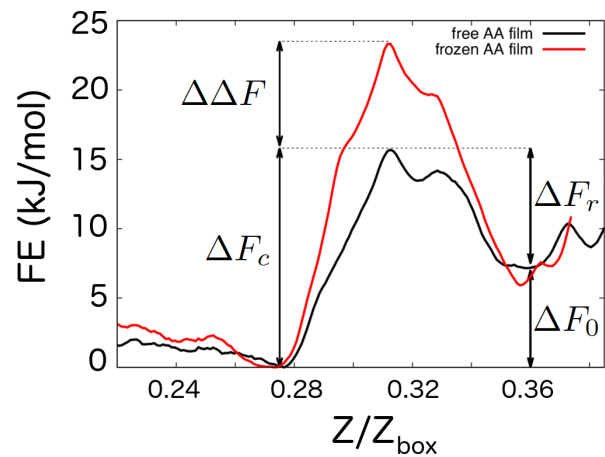

FIG. 4. FEPs associated with the passage of the *free* methane molecule across the interfacial layer, obtained within the US/ABMD framework. The AA surface density is ≈ 0.67 molecules/nm^2. The *x*-axis corresponds to the *Z*-Cartesian coordinate of methane expressed in reduced units, Z/Z_{box}, with Z_{box} the size of the simulation box along the Z direction. We show the *minimal* FE pathways obtained when the AA molecules are either frozen (red) or free (black). The activation energies associated with methane capture and escape, ΔF_c and ΔF_r, are ≈ 15.5 kJ/mol and ≈ 7 kJ/mol, respectively.
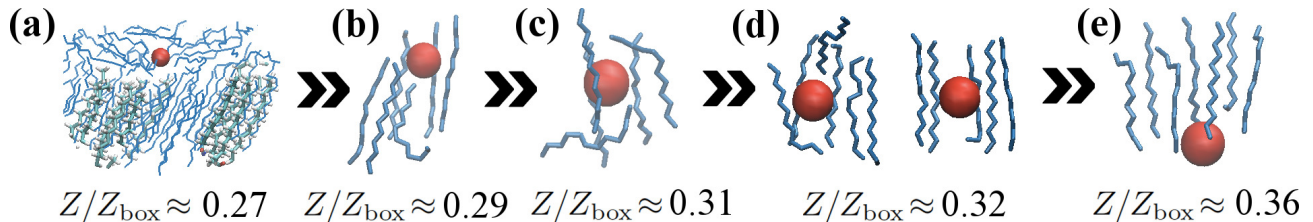
FIG. 5. Sequence of simulation snapshots representing the transport mechanism of the methane molecule (red sphere) along the *minimal* FE pathway across the flat interfacial layer composed of a mixture of AA and dodecane (blue molecules). The bulk hydrocarbon phase and the sII hydrate are not shown for clarity. The AA layer is only shown in (a). The methane molecule initially starts in the bulk hydrocarbon phase, above the AA layer (a). The methane molecule then enters the interfacial layer through two oil molecules (b). As the methane goes farther across the interfacial layer, the oil molecules below the methane molecule bend, eventually forming a *cage* surrounding the methane molecule (c). As the methane travels farther down, one oil molecule forming the gate begins pushing the methane molecule. At that stage, the system evolves between two states corresponding to a closed or opened gate below the methane molecule (d). Eventually, the methane molecule is driven underneath the AA layer (e).

ters the AA layer between two hydrocarbon molecules. As the methane travels farther across the interfacial layer, an energy barrier arises as the oil molecules are displaced from the methane pathway. The transport proceeds until one oil molecule cannot be pushed farther down ($0.27 \lesssim Z/Z_{\text{box}} \lesssim 0.31$). At these conditions, the oil molecule being displaced bends, eventually forming a *cage* surrounding the methane molecule ($Z/Z_{\text{box}} \approx 0.31$). This corresponds to the high energy transition region in the FE landscape. From this point on, the hydrocarbon forming the *cage* effectively contributes to actively pushing the methane towards the hydrate. The system evolves between two states corresponding to a closed or opened *gate* below the methane molecule ($0.31 \lesssim Z/Z_{\text{box}} \lesssim 0.34$). Once the methane molecule overcomes this *transition state*, it is pushed down underneath the AA layer ($Z/Z_{\text{box}} \approx 0.35$). The methane molecule then reaches the local minimum corresponding to the water layer between the AA layer and the hydrate. This analysis does not explore further transport through the water film.

Dynamical Properties

To estimate the transition rates along the FE pathway, we considered the Kramers theory [117–122], which is based on the inertial Langevin equation [123]:

$$m\ddot{q} = -\frac{\partial V}{\partial q} - m\gamma\dot{q} + R(t)\,. \tag{4}$$

In Eq. 4, q represents the reaction coordinate, m is the reduced mass for the reaction coordinate, γ is the friction coefficient, and $V(q)$ is a PMF. $R(t)$ is a random force with zero mean that satisfies the fluctuation theorem [124]. In the presented case, Eq. 4 is applied to the methane molecule, the reaction coordinate is the Z-Cartesian coordinate, m represents the methane

molecule mass, and $V(q)$ is the PMF discussed in Figure 4. The escaping/capture rates can be described within the Kramers theory framework in terms of diffusion across a FE barrier of height ΔF when the barrier (and local minima) are modeled as parabolic potentials [121]:

$$V(q) = V_{TS} - \frac{1}{2}m\omega_{TS}^2(q - q_{TS})^2\,. \tag{5}$$

The Kramers theory provides a physical derivation of the reaction rate constants in terms of the shape of the energy profile. From intermediate to high friction regimes, the reaction rate, k, is given as:

$$k = \frac{\gamma}{\omega_{TS}}\left(\sqrt{\frac{1}{4} + \frac{\omega_{TS}^2}{\gamma^2}} - \frac{1}{2}\right)\frac{\omega_0}{2\pi}e^{-\Delta F/k_B T} \tag{6}$$

where ω_0 and ω_{TS} represent the stiffness of the potential well and the barrier, respectively, $\gamma = 6\pi\eta R/m$ the friction coefficient, with η the effective viscosity, and ΔF the FE barrier. Figure 6 shows the FEP fitted using harmonic potentials at the local minimum and maximum. This yields $\omega_0 \approx 100\times10^{13}\ s^{-1}$ and $\omega_{TS} \approx 230\times10^{13}\ s^{-1}$ (cf. details in the SI). One important parameter is the effective viscosity η. Because of confinement of the liquid hydrocarbon at the interface, the effective viscosity is intrinsically different from its bulk value [116] (≈ 2 mPa.s at 277 K and 20 MPa). Singer and Pollock [116] showed that the effective viscosity can increase by several orders of magnitude when dodecane molecules are confined in a space approaching the molecular dimension of the liquid hydrocarbon. Eventually, they observed the divergence of the effective viscosity. Considering $\eta \approx 10^2 - 10^5$ Pa.s [116], one obtains a lower boundary for the friction coefficient, $\gamma > 15 \times 10^{18}\ s^{-1} >> \omega_{TS}$, characteristic of the strong friction regime of interest here. In this limit, Eq. 6 simplifies to [121]

$$k = \frac{\omega_0\omega_{TS}}{2\pi\gamma}e^{-\Delta F/k_B T}\,. \tag{7}$$

This approximation is often used to interpret, for instance, the time scale characteristic for protein or DNA conformational dynamics [89, 125]. Considering the parameter values discussed previously, one obtains a characteristic time scale for methane escape from the aqueous film near the hydrate to the hydrocarbon liquid phase, across the AA film, $\tau_{esc} \approx 0.01 - 1$ μs.

Building on the recent method of Parrinello, Salvalaglio, and Tiwary [105, 106], we extend the metaD scope to assess numerically τ_{esc}. We indicate our numerical result as $\tau_{esc}^{(\mathrm{num})}$ in what follows. WT-metaD was performed using the Z coordinate as CV with the parameters reported in the Methods section. The statistics for $\tau_{esc}^{(\mathrm{num})}$ conformed to a Poisson distribution with mean $\mu = 0.08 \pm 0.02$ μs and variance $\lambda = 0.09$ μs. The statistics obeys a two-sample KS test with p-value equal to 0.52. This numerical result confirms the reliability of the choice of the Z-Cartesian coordinate as a collective variable in the US framework (cf. discussion in the SI) and is comparable to the estimation derived from the Kramers theory with a friction coefficient $\gamma \approx 10^4$ Pa.s.

Finally we quantified the characteristic time scale for methane capture (from the hydrocarbon to the hydrate surface) along the *minimal* FE path, τ_{cap}. As shown in Figure 6, no confinement was present above the AA layer ($Z/Z_{\mathrm{box}} < 0.27$). Thus the entropic effect would dominate, and the associated rate of capture would tend to infinity. To correct for this, an external potential was added at $Z/Z_{\mathrm{box}} \approx 0.25$, similar to the FE barrier observed for $Z/Z_{\mathrm{box}} \in [0.27, 0.31]$. This external potential would represent, for instance, a free methane molecule confined between two AA layers. The statistics of our numerical analysis for $\tau_{cap}^{(\mathrm{num})}$ conformed to a Poisson distribution with mean $\mu = 0.35 \pm 0.15$ μs and variance $\lambda = 0.49$ μs, and followed a two-sample KS test with
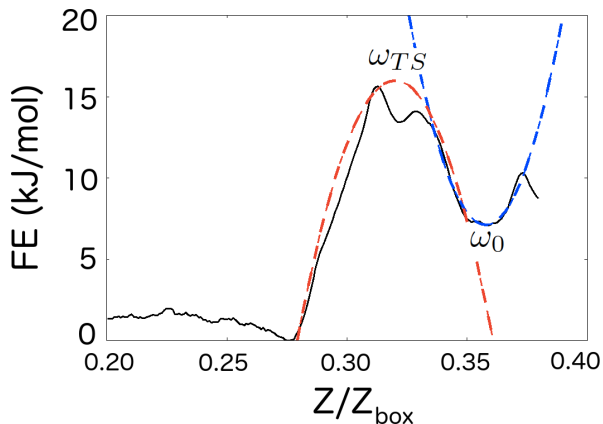

FIG. 6. Fitting of the FEP within parabolic potentials to extract parameters for the Kramers theory. The nonlinear least-squares Marquardt-Levenberg algorithm was implemented obtaining $\omega_0 \approx 100 \times 10^{13}$ s^{-1} and $\omega_{TS} \approx 230 \times 10^{13}$ s^{-1}.

p-value equal to 0.51 (cf details in the SI).

Intermediate free-energy pathway

To conclude this analysis, we considered the *intermediate* path defined in Figure 3, which presents a similar FE barrier associated with methane capture but a deeper energy basin at $Z/Z_{\mathrm{box}} \approx 0.35$ along with a higher FE barrier associated with methane escape. We reconstructed the accurate FEP within the US/ABMD framework and obtained the respective values for $\omega_{TS} \approx 100 \times 10^{13}$ s^{-1} and $\omega_0 \approx 130 \times 10^{13}$ s^{-1}. The details are reported in the SI. Considering Eq. 7 with $\gamma \approx 10^4$ Pa.s, we obtained a characteristic time scale for methane escape, $\tau_{esc} \approx 40$ μs. The estimated characteristic time scale for methane capture was similar to that obtained in correspondence of the *minimal* path.

Discussion

The extensive simulations discussed previously allowed for identification of three possible pathways that a methane molecule can follow to diffuse from the hydrocarbon phase to the hydrate structure across the interfacial film rich in AAs. We focused on the pathway that showed the minimal FE barrier and we quantified accurately the FEPs using a combination of enhanced sampling techniques. This allowed us to reveal the molecular mechanism responsible for the FE barrier. Interpreting the FEP within the Kramers theory allowed us to extract the time constant that quantifies the escape rate of the methane across the AA film. The result is consistent with estimations from a direct metaD estimate, which supports the reliability of our approach.

We showed that the FE barrier comes from local flexibility of the liquid hydrocarbon molecules within the AA film. The flexibility of the oil molecules is impacted by the rigidity of the AA molecules. We observed that the interaction of the methane molecule with the AA short tail can increase the stability of the system and invert its thermodynamic stability. Increasing the AA surface density leads to an increase in the heigh of the FE barrier, improving eventually the efficiency of the interfacial layer in limiting the transport of methane.

The characteristic time obtained from this study can be compared with the experimental growth rate of methane hydrate film at flat methane/water interface. Sun et al. [126], and more recently Li et al. [25] reported growth characteristic time $\tau^{\mathrm{exp}} \approx 1 - 5$ μs, depending on the degree of supercooling considered in the experiments. This is one order of magnitude higher than the escaping time obtained in our simulations for the *minimal* FE pathway and one order of magnitude lower than that obtained for the *intermediate* FE pathway. These

data suggest that ordering of the long AA tails observed for the AAs considered here can provide effective barriers to methane transport. Further, the results suggest that the short tails of the AAs can be designed to enhance the stability of methane near the growing hydrate.

The new physical insights discussed in this paper could be useful for a variety of applications. For instance, several research groups focus on the interplay between design and performance of AAs at the microscopic scale. Accounting for the collective effect of new AAs could allow us to infer their use in practical applications, which addresses the current needs.

ACKNOWLEDGEMENTS

---

* Corresponding author: francois.sicard@free.fr.

[1] C.A. Koh, R.E. Westacott, W. Zhang, K. Hirachand, J.L. Creek, and A.K. Soper, "Mechanisms of gas hydrate formation and inhibition," Fluid Phase Equilib. **194-197**, 143–151 (2002).

[2] M.A. Kelland, "History of the development of low dosage hydrate inhibitors," Energy Fuels **20**, 825–847 (2006).

[3] E. Sloan and C.A. Koh, Clathrate hydrates of natural gases, 3rd Ed. (CRC Press: Boca Raton, Florida, 2008).

[4] M.R. Walsh, C.A. Koh, E.D. Sloan, A.K. Sum, and D.T. Wu, "Microsecond simulations of spontaneous methane hydrate nucleation and growth," Science **326**, 1095–1098 (2009).

[5] V.K. Michalis, J. Costandy, I.N. Tsimpanogiannis, A.K. Stubos, and I.G. Economou, "Prediction of the phase equilibria of methane hydrates using the direct phase coexistence methodology," J. Chem. Phys. **142**, 044501 (2015).

[6] P.G. Brewer, F.M. Orr Jr., G. Friederich, K.A. Kvenvolden, D.L. Orange, J. McFarlane, and W. Kirkwood, "Deep-ocean field test of methane hydrate formation from a remotely operated vehicle," Geology **25**, 407–410 (1997).

[7] A.K. Sum, C.A. Koh, and E.D. Sloan, "Clathrate hydrates: From laboratory science to engineering practice," Ind. Eng. Chem. Res. **48**, 7457–7465 (2009).

[8] K. Kaiho, T. Arinobu, R. Ishiwatari, H.E.G. Morgans, H. Okada, N. Takeda, K. Tazaki, G. Zhou, Y. Kajiwara, R. Matsumoto, A. Hirai, N. Niitsuma, and H. Wada, "Latest paleocene benthic foraminiferal extinction and environmental changes at tawanui, new zealand," Paleoceanography **11**, 447 (1996).

[9] K.S. Park, Z. Ni, A.P. Côté, J.Y. Choi, R. Huang, F.J. Uribe-Romo, H.K. Chae, M. OKeeffe, and O.M. Yaghi, "Exceptional chemical and thermal stability of zeolitic imidazolate frameworks," Proc. Natl. Acad. Sci. U.S.A. **103**, 12690 (2006).

[10] E.D. Sloan, "Fundamental principles and applications of natural gas hydrates," Nature **426**, 353 (2003).

[11] L.J. Florusse, C.J. Peters, J. Schoonman, K.C. Hester, C.A. Koh, S.F. Dec, K.N. Marsh, and E.D. Sloan, "Stable low-pressure hydrogen clusters stored in a binary clathrate hydrate," Science **306**, 469 (2004).

[12] W.L. Mao, H.K. Mao, A.F. Goncharov, V.V. Struzhkin, Q. Guo, J. Hu, J. Shu, R.J. Hemley, M. Somayazulu, and Y. Zhao, "Hydrogen clusters in clathrate hydrate," Science **297**, 2247 (2002).

[13] T. Ogawa, T. Ito, K. Watanabe, K. ichi Tahara, R. Hiraoka, J. ichi Ochiai, R. Ohmura, and Y.H. Mori, "Development of a novel hydrate-based refrigeration system: A preliminary overview," Appl. Therm. Eng. **26**, 2157 (2006).

[14] C.R. Fisher, I.R. MacDonald, R. Sassen, C.M. Young, S.A. Macko, S. Hourdez, R.S. Carney, S. Joye, and E. McMullin, "Methane ice worms: Hesiocaeca methanicola colonizing fossil fuel reserves." Naturwissenschaften **87**, 184 (2000).

[15] D.J. Milton, "Carbon dioxide hydrate and floods on mars," Science **183**, 654 (1974).

[16] E.D. Sloan, C. Koh, A.K. Sum, A.L. Ballard, J. Creek, M. Eaton, J. Lachance, N. McMullen, T. Palermo, G. Shoup, and L. Talley, Natural Gas Hydrates in Flow Assurance, 3rd Ed. (Gulf Professional Pub./Elsevier:Burlington, Massachusetts, 2011) pp. 1–200.

[17] J.W. Mullin, Chapter 5: Nucleation. In Crystallization, 4th Ed. (Butterworth-Heinemann: Oxford (UK), 2011).

[18] E.M. Freer, M.S. Selim, and E.D. Sloan, "Methane hydrate film growth kinetics," Fluid Phase Equilib. **185**, 65–75 (2001).

[19] D.J. Turner, Clathrate Hydrate Formation in Water-in-oil Dispersio (Ph.D. Thesis, Colorado School of Mines, Golden (CO), April 2005).

[20] E.D. Sloan, Hydrate Engineering (Society of Petroleum Engineers, Richardson (TX), 2000).

[21] J.M. Lee, S.J. Cho, J.D. Lee, P. Linga, K.C. Kang, and J. Lee, "Insights into the kinetics of methane hydrate formation in a stirred tank reactor by in situ raman spectroscopy," Energy Technol. **3**, 925–934 (2015).

[22] O. Fandino and L. Ruffine, "Methane hydrate nucleation and growth from the bulk phase: Further insights into their mechanisms," Fuel **117**, 442–449 (2014).

[23] S.A. Kulkarni, S.S. Kadam, H. Meekes, A.L. Stankiewicz, and J.H. ter Horst, "Crystal nucleation kinetics from induction times and metastable zone widths," Cryst. Growth Des. **13**, 2435–2440 (2013).

[24] H. Abay and T.M. Svartaas, "Multicomponent gas hydrate nucleation: The effect of the cooling rate and composition," Energy Fuels **25**, 42–51 (2011).

[25] S. Li, C. Sun, B. Liu, Z. Li, G. Chen, and A.K. Sum, "New observations and insights into the morphology and growth kinetics of hydrate films," Sci. Rep. **4**, 1 (2014).

[26] W. Ke and M.A. Kelland, "Kinetic hydrate inhibitor studies for gas hydrate systems: A review of experimental equipment and test methods," Energy Fuels **30**, 10015–10028 (2016).

[27] D. Yuhara, B.C. Barnes, D. Suh, B.C. Knott, G.T. Beckham, K. Yasuoka, D.T. Wu, and A.K. Sum, "Nucleation rate analysis of methane hydrate from molecular dynamics simulation," Faraday Discuss. **179**, 463–474 (2015).

[28] C. Moon, R.W. Hawtin, and P.M. Rodger, "Nucleation and control of clathrate hydrates: Insights from simulation," Faraday Discuss. **136**, 367–382 (2007).

[29] J. Vatamanu and P.G. Kusalik, "Molecular insights into the heterogeneous crystal growth of si methane hydrate," J. Phys. Chem. B **26**, 15896–15904 (2006).

[30] A.K. Sum, C.A. Koh, and E.D. Sloan, "Developing a comprehensive understanding and model of hydrate in multiphase flow: From laboratory measurements to field applications," Energy Fuels **26**, 4046–4052 (2012).

[31] C.P. Ribeiro Jr. and P.L.C. Large, "Modelling of hydrate formation kinetics: State-of-the-art and future directions," Chem. Eng. Sci. **63**, 2007–2034 (2008).

[32] L. Zhang, C. Zhang, H. Huang, D. QI, Y. Zhang, S. Ren, Z. Wu, and M. Fang, "Gas hydrate risks and prevention for deep water drilling and completion: A case study of well qdn-x in qiongdongnan basin, south china sea," Petrol. Explor. Develop. **41**, 824–832 (2014).

[33] J.P. Lederhos, J.P. Long, A. Sum, R.L. Christiansen, and E.D. Sloan, "Effective kinetic inhibitors for natural gas hydrates," Chem. Eng. Sci. **51**, 1221–1229 (1996).

[34] H. Zhao, M. Sun, and A.Firoozabadi, "Anti-agglomeration of natural gas hydrates in liquid condensate and crude oil at constant pressure conditions," Fuel **180**, 187–193 (2016).

[35] E.D. Sloan, "Method for controlling clathrate hydrates in fluid systems," U.S. Patent US5880319 A (May 25, 1994).

[36] T. Bui, A. Phan, D. Monteiro, Q. Lan, M. Ceglio, E. Acosta, P. Krishnamurthy, and A. Striolo, "Evidence of structure-performance relation for surfactant used as antiagglomerant for hydrate management," Langmuir **33**, 2263–2274 (2017).

[37] M.A. Kelland, T.M. Svartaas, and L.D. Andersen, "Gas hydrate antiagglomerant properties of polypropoxylates and some other demulsifiers," J. Pet. Sci. Eng. **64**, 1–10 (2009).

[38] Z. Aman, E.D. Sloan, A.K. Sum, and C.A. Koh, "Adhesion force interactions between cyclopentane hydrate and physically and chemically modified surfaces," Phys. Chem. Chem. Phys. **16**, 25121–25128 (2014).

[39] ecular mechanisms responsible for hydrate anti-agglomerant performance, "Emulsification in viscoelastic media," Phys. Chem. Chem. Phys. **18**, 24859–24871 (2016).

[40] T. Bui, F. Sicard, D. Monteiro, Q. Lan, M. Ceglio, C. Burress, and A. Striolo, "Molecular mechanisms by which anti-agglomerants affect gas hydrate growth," Nano Lett., submitted for publication (2018).

[41] M.L. Zanota, C. Dicharry, and A. Graciaa, "Hydrate plug prevention by quaternary ammonium salts," Energy Fuels **19**, 584–590 (2005).

[42] J. Chen, C. Sun, B. Peng, B. Liu, S. Si, and M. Jia et al., "Screening and compounding of gas hydrate anti-agglomerants from commercial additives through morphology observation," Energy Fuels **27**, 2488–2496 (2013).

[43] M.A. Kelland, T.M. Svartaas, J. Ovsthus, T. Tomita, and J. Chosa, "Studies on some zwitterionic surfactant gas hydrate anti-agglomerants," Chem. Eng. Sci. **61**, 4048–4059 (2006).

[44] M. Sun, Y. Wang, and A. Firoozabadi, "Effectiveness of alcohol cosurfactants in hydrate antiagglomeration," Energy Fuels **26**, 5626–5632 (2012).

[45] J. Chen, J. Liu, C. Sun, M. Jia, and B. Liu et al., "Insights into methane hydrate formation, agglomeration, and dissociation in water + diesel oil dispersed system," Energy Convers. Manage. **86**, 886–891 (2014).

[46] J. Chen, Y. Wang, C. Sun, F. Li, N. Ren, M. Jia, K.L. Yan, Y.-N. Lv, B. Liu, and G.-J. Chen, "Evaluation of gas hydrate anti-agglomerant based on laser measurement," Energy Fuels **29**, 122–129 (2015).

[47] S. Gao, "Hydrate risk management at high watercuts with anti-agglomerant hydrate inhibitors," Energy Fuels **23**, 2118–2121 (2009).

[48] M.A. Kelland, Production Chemicals for the Oil and Gas Industry, (CRC Press: Boca Raton, Florida, 2014).

[49] M. Lauricella, S. Meloni, N.J. English, B. Peters, and G. Ciccotti, "Methane clathrate hydrate nucleation mechanism by advanced molecular simulations," J. Phys. Chem. C **118**, 22847–22857 (2014).

[50] M. Lauricella, S. Meloni, S. Liang, N.J. English, P.G. Kusalik, and G. Ciccotti, "Clathrate structure-type recognition: Application to hydrate nucleation and crystallisation," J. Chem. Phys. **142**, 244503 (2015).

[51] K.W. Hall, S. Carpendale, and P.G. Kusalik, "Evidence from mixed hydrate nucleation for a funnel model of crystallization," Proc. Nat. Acad. Soc. U.S.A. **113**, 12041–12046 (2016).

[52] F. Jimenez-Angeles and A. Firoozabadi, "Anti-agglomeration in clathrate hydrates by molecular dynamics simulations," Proceeding of the 9th International Conference on Gas Hydrates, Denver, Colorado, USA (June 25-30, 2017).

[53] M. Bellucci, M. Walsh, and B. Trout, "Molecular dynamics analysis of surface adsorption in natural gas hydrates," Proceeding of the 9th International Conference on Gas Hydrates, Denver, Colorado, USA (June 25-30, 2017).

[54] A. Laio and M. Parrinello, "Escaping free-energy minima," Proc. Nat. Acad. Soc. U.S.A. **99**, 1256212566 (2002).

[55] G.M. Torrie and J.P.Valleau, "Nonphysical sampling distributions in monte carlo free-energy estimation: Umbrella sampling," J. Comput. Phys. **23**, 187–199 (1977).

[56] M.J. Abraham, T. Murtola, R. Schulz, S. Páll, J.C. Smith, B. Hess, and E. Lindahl, "Gromacs: High performance molecular simulations through multi-level parallelism from laptops to supercomputers," SoftwareX **1-2**, 19–25 (2015).

[57] J.L.F. Abascal, E. Sanz, R. Fernández Garcia, and C. Vega, "A potential model for the study of ices and amorphous water: Tip4p/ice," J. Chem. Phys. **122**, 234511 (2005).

[58] G.A. Tribello, M. Bonomi, D. Branduardi, C. Camilloni, and G. Bussi, "Plumed 2: New feathers for an old bird," Comput. Phys. Comm. **185**, 604–613 (2014).

[59] L. Jensen, K. Thomsen, N. von Solms, S. Wierzchowski, M.R. Walsh, C.A. Koh, E.D. Sloan, D.T. Wu, and A.K. Sum, "Calculation of liquid water-hydrate-methane vapor phase equilibria from molecular simulations," J. Phys. Chem. B **114**, 5775–5782 (2010).

[60] S. Alireza Bagherzadeh, S. Alavi, J.A. Ripmeester, and P. Englezos, "Why ice-binding type i antifreeze protein acts as a gas hydrate crystal inhibitor," Phys. Chem. Chem. Phys. **17**, 9984–9990 (2015).

[61] M.M. Conde and C. Vega, "Determining the three-phase coexistence line in methane hydrates using computer simulations," J. Chem. Phys. **133**, 064507 (2010).

[62] M.G. Martin and J.I. Siepmann, "Transferable potentials for phase equilibria. 1. united-atom description of n-alkanes," J. Phys. Chem. B **102**, 2569–2577 (1998).

[63] J. Wang, R.M. Wolf, J.W. Caldwell, P.A. Kollman, and D.A. Case, "Transferable potentials for phase equilibria. 1. united-atom description of n-alkanes," J. Comput. Chem. **25**, 1157–1174 (2004).

[64] D.A. Case, J.T. Berryman, R.M. betz, Q. Cai, D.S. Cerutti, T.E. Cheatham, T.A. Darden, R.E. Duke, H. Gohlke, A.W. Goetz, S. Gusarov, N. Homeyer, P. Janowski, J. Kaus, I. Lolossváry, A. Kovalenko, T.S. Lee, S. LeGrand, T. Luchko, R. Luo, B. Madej, K.M. Merz, F. Paesani, D.R. Roe, A. Roitberg, C. Sagui, R. Salomon-Ferrer, G. Seabra, C.L. Simmerling, W. Smith, J. Swails, R.C. Walker, J. Wang, R.M. Wolf, X. Wu, and P.A. Kollman, <u>AMBER 14</u> (University of California: San Francisco, California, 2014).

[65] D.E. Smith and L.X. Dang, "Computer simulations of nacl association in polarizable water," J. Chem. Phys. **100**, 3757–3766 (1994).

[66] H.A. Lorentz, "Ueber die anwendung des satzes vom virial in der kinetischen theorie der gase," Ann. Phys. **248**, 127–136 (1881).

[67] D. Berthelot, "Sur le mélange des gaz," Compt. Rendus **126**, 1703–1706 (1898).

[68] T. Darden, D. York, and L. Pedersen, J. Chem. Phys. **98**, 10089–10092 (1993).

[69] U. Essmann, L. Perera, and M.L. Berkowitz, "A smooth particle mesh ewald method," J. Chem. Phys. **103**, 8577 (1995).

[70] M. Kawata and U. Nagashima, Chem. Phys. Lett. **340**, 165–172 (2001).

[71] F. Takeuchi, M. Hiratsuka, R. Ohmura, S. Alavi, A.K. Sum, and K. Yasuoka, "Water proton configurations in structures i, ii, and h clathrate hydrate unit cells," J. Chem. Phys. **138**, 124504 (2013).

[72] H.J.C. Berendsen, J.P.M. Postma, W.F. van Gunsteren, A. DiNola, and J. R. Haak, "Molecular dynamics with coupling to an external bath," J. Chem. Phys. **81**, 3684–3690 (1984).

[73] S. Pronk, S.Páll, R. Schulz, P. Larsson, P. Bjelkmar, R. Apostolov, M.R. Shirts, J.C. Smith, P.M. Kasson, D. van der Spoel, B. Hess B, and E. Lindahl, "Gromacs 4.5: a high-throughput and highly parallel open source molecular simulation toolkit," Bioinformatics **29**, 845–854 (2013).

[74] D.J. Evans and B.L. Holian, "The nosehoover thermostat," J. Chem. Phys. **83**, 4069 (1985).

[75] M. Parrinello and A. Rahman, "Polymorphic transitions in single crystals: a new molecular dynamics method," J. Appl. Phys. **52**, 7182–7190 (1981).

[76] G. Bussi, D. Donadio, and M. Parrinello, "Canonical sampling through velocity rescaling," J. Chem. Phys. **126**, 014101 (2007).

[77] S.A. Adcockand J.Andrew McCammon, "Molecular dynamics: Survey of methods for simulating the activity of proteins," Chem. Rev. **106**, 1589–1615 (2006).

[78] V. Spiwok, Z. Sucur, and P. Hosek, "Enhanced sampling techniques in biomolecular simulations," Biotechnology Adv. **33**, 1130–1140 (2015).

[79] R.C. Bernardi, M.C.R. Melo, and K. Schulten, "Enhanced sampling techniques in molecular dynamics simulations of biological systems," Biochim. Biophys. Acta. **1850**, 872–877 (2015).

[80] T. Maximova, R. Moffatt, R. Nussinov, and A. Shehu, "Principles and overview of sampling methods for modeling macromolecular structure and dynamics," PLoS Comput. Biol. **12**, e1004619 (2016).

[81] F. Pietrucci, "Strategiesfor the exploration of free energy landscapes: Unity in diversity and challenges ahead," Rev. Phys. **2**, 32–45 (2017).

[82] A. Laio and F.L. Gervasio, "Metadynamics: a method to simulate rare events and reconstruct the free energy in biophysics, chemistry and material science," Rep. Prog. Phys. **71**, 126601 (2008).

[83] A. Barducci, M. Bonomi, and M. Parrinello, "Metadynamics," WIREs Comput. Mol. Sci. **1**, 826–843 (2011).

[84] L. Sutto, S. Marsili, and F.L. Gervasio, "New advances in metadynamics," WIREs Comput. Mol. Sci. **2**, 771–779 (2012).

[85] J. Kastner, "Umbrella sampling," WIREs Comput. Mol. Sci. **1**, 932–942 (2011).

[86] A. Barducci, R. Chelli, P. Procacci, V. Schettino, F.L. Gervasio, and M. Parrinello, "Metadynamics simulation of prion protein: β-structure stability and the early stages of misfolding," J. Am. Chem. Soc. **128**, 2705–2710 (2006).

[87] L. Sutto and F.L. Gervasio, "Effects of oncogenic mutations on the conformational free-energy landscape of egfr kinase," Proc. Nat. Acad. Soc. **110**, 10616–10621 (2013).

[88] F. Sicard and P. Senet, "Reconstructing the free-energy landscape of met-enkephalin using dihedral principal component analysis and well-tempered metadynamics," J. Chem. Phys. **138**, 235101 (2013).

[89] F. Sicard, N. Destainville, and M. Manghi, "Dna denaturation bubbles: Free-energy landscape and nucleation/closure rates," J. Chem. Phys. **142**, 034903 (2015).

[90] F. Giberti, M. Salvalaglio, and M. Parrinello, "Metadynamics studies of crystal nucleation," IUCrJ **2**, 256–266 (2015).

[91] M. Salvalaglio, M. Mazzotti, and M. Parrinello, "Urea homogeneous nucleation mechanism is solvent dependent," Faraday Discus. **179**, 291–307 (2015).

[92] I. Gimondi and M. Salvalaglio, "co_2 packing polymorphism under pressure: mechanism and thermodynamics of the i-iii polymorphic transition," J. Chem. Phys. **147**, 114502 (2017).

[93] A. Barducci, G. Bussi, and M. Parrinello, "Well-tempered metadynamics: A smoothy converging and tunable free-energy method," Phys. Rev. Lett. **100**, 020603 (2008).

[94] J.F. Dama, M. Parrinello, and G.A. Voth, "Well-tempered metadynamics converges asymptotically,"

Phys. Rev. Lett. **112**, 240602 (2014).

[95] Y. Zhang and G.A. Voth, "Combined metadynamics and umbrella sampling method for the calculation of ion permeation free energy profiles," J. Chem. Theory Comput. **7**, 2277–2283 (2011).

[96] M. Nishizawa and K. Nishizawa, "Molecular dynamics simulation analysis of membrane defects and pore propensity of hemifusion diaphragms," Biophys. J. **104**, 1038–1048 (2013).

[97] E. Paci and M. Karplus, "Forced unfolding of fibronectin type 3 modules: An analysis by biased molecular dynamics simulations," J. Mol. Biol. **288**, 441–459 (1999).

[98] M. Marchi and P. Ballone, "Adiabatic bias molecular dynamics: A method to navigate the conformational space of complex molecular systems," J. Chem. Phys. **110**, 3697–3702 (1999).

[99] C. Camilloni, R.A. Broglia, and G. Tiana, "Hierarchy of folding and unfolding events of protein g, ci2, and acbp from explicit-solvent simulations," J. Chem. Phys. **134**, 045105 (2011).

[100] F. Sicard and A. Striolo, "Numerical analysis of pickering emulsion stability: insights from abmd simulations," Faraday Discuss. **191**, 287–304 (2016).

[101] T.W. Allen, O.S. Andersen, and B. Roux, "Energetics of ion conduction through the gramicidin channel," Proc. Nat. Acad. Sci. U.S.A. **101**, 117–122 (2004).

[102] F. Zhu and G. Hummer, "Theory and simulation of ion conduction in the pentameric glic channel," J. Chem. Theory Comput. **8**, 3759–3768 (2012).

[103] A. Grossfiled, "Wham: the weighted histogram analysis method, version 2.0.9," http://membrane.urmc.rochester.edu/content/wham.

[104] J.S. Hub, B.L. de Groot, and D. van der Spoel, "$g_w hams$ - a free weighted histogram analysis implementation including robust error and autocorrelation estimates," J. Chem. Theory Comput. **6**, 3713–3720 (2010).

[105] P. Tiwary and M. Parrinello, "From metadynamics to dynamics," Phys. Rev. Lett. **111**, 230602 (2013).

[106] M. Salvalaglio, P. Tiwary, and M. Parrinello, "Assessing the reliability of the dynamics reconstructed from metadynamics," J. Chem. Theory Comput. **10**, 1420–1425 (2014).

[107] J. Schneider and K. Reuter, "Efficient calculation of microscopic dissolution rate constants: The aspirinwater interface," J. Phys. Chem. Lett. **5**, 3859–3862 (2014).

[108] M. Salvalaglio, C. Perego, F.Giberti, M. Mazzotti, and M. Parrinello, "Molecular-dynamics simulations of urea nucleation from aqueous solution," Proc. Nat. Acad. Sci. U.S.A. **112**, E6–E14 (2015).

[109] P. Tiwary, V. Limongelli, M. Salvalaglio, and M. Parrinello, "Kinetics of proteinligand unbinding: Predicting pathways, rates, and rate-limiting steps," Proc. Nat. Acad. Sci. U.S.A. **112**, E386–E391 (2015).

[110] P. Tiwary, J. Mondal, J.A. Morrone, and B.J. Berne, "Role of water and steric constraints in the kinetics of cavity-ligand unbinding," Proc. Nat. Acad. Soc. U.S.A. **112**, 12015–12019 (2015).

[111] P.M. Piaggi, O. Valssonbc, and M. Parrinello, "A variational approach to nucleation simulation," Faraday Discuss. **195**, 557–568 (2016).

[112] D. Bochicchio, M. Salvalaglio, and G.M. Pavan, "Into the dynamics of a supramolecular polymer at submolecular resolution," Nat. Commun. **8**, 147 (2017).

[113] V. Limongelli, L. Marinelli, S. Cosconati, C. La Motta, S. Sartini, L. Mugnaini, F. Da Settimo, E. Novellino, and M. Parrinello, "Sampling protein motion and solvent effect during ligand binding," Proc. Natl. Acad. Sci. U.S.A. **109**, 1467–1472 (2012).

[114] J. Yang, M. Bonomi, C. Calero, and J. Mart, "Free energy landscapes of sodium ions bound to dmpccholesterol membrane surfaces at infinite dilution," Phys. Chem. Chem. Phys. **18**, 9036–9041 (2016).

[115] S. Bhakat and P. Soderhjelm, "Resolving the problem of trapped water in binding cavities: prediction of hostguest binding free energies in the sampl5 challenge by funnel metadynamics," J. Comput. Aided Mol. Des. **31**, 119–132 (2017).

[116] S. Granick, Fundamentals of Friction, Macroscopic and Microscopic (I.L. Singer and H. Pollock Eds.; Springer Netherlands, 1992) pp. 387–401.

[117] H.A. Kramers, "Brownian motion in a field of force and the diffusion model of chemical reactions," Physica (Amsterdam) **7**, 284 (1940).

[118] P. Hanggi, P. Talkner, and M. Borkovec, "Reaction-rate theory: fifty years after kramers," Rev. Mod. Phys. **82**, 251–341 (1990).

[119] E. Pollak and P. Talkner, "Reaction rate theory: What it was, where is it today, and where is it going?" Chaos **15**, 026116 (2005).

[120] H.-X. Zhou, "Rate theories for biologist," Quaterly Rev.Biophys. **43**, 219–293 (2010).

[121] B. Peters, Reaction Rate Theory and Rare Events, 1st Ed. (Elsevier: Amsterdam, The Netherlands, 2017).

[122] F. Sicard, "Computing transition rates for rare event: When kramers theory meets free energy landscape," arXiv:1803.03490 [cond-mat.stat-mech] (2018).

[123] W.T Coffey and Y.P. Kalmykov, The Langevin Equation: With Applications to Stochastic Problems Vol. 27 (World Scientific Publishing Company: Singapore, 2012).

[124] U. Marini, B. Marconi, A. Puglisiand L. Rondoni, and A. Vulpiani, "Fluctuation-dissipation: Response theory in statistical physics," Phys. Rep. **461**, 111–195 (2008).

[125] H. Yu, A.N. Gupta, X. Liu, K. Neupane, A.M. Brigley, I. Sosova, and M.T Woodside, "Energy landscape analysis of native folding of the prion protein yields the diffusion constant, transition path time and rates," Proc. Nat. Acad. Sci. U.S.A. **109**, 14452–14457 (2012).

[126] C.Y. Sun, B.Z. Peng, A. Dandekar, Q.L. Ma, and G.J. Chen, "Studies on hydrate film growth," Annu. Rep. Prog. Chem., Sect. C **106**, 77–100 (2010).